The Cryosphere Discuss., 9, 2101–2133, 2015
www.the-cryosphere-discuss.net/9/2101/2015/
doi:10.5194/tcd-9-2101-2015

The Cryosphere Discussions
Open Access

An analytical model for wind-driven Arctic summer sea ice drift

H.-S. Park[1] and A. L. Stewart[2]

[1]Korea Institute of Geoscience and Mineral Resources, Daejeon, South Korea
[2]Department of Atmospheric and Oceanic Sciences, University of California, Los Angeles, CA, USA

Received: 12 January 2015 – Accepted: 11 March 2015 – Published: 27 March 2015

Correspondence to: H.-S. Park (hspark1@gmail.com)

Published by Copernicus Publications on behalf of the European Geosciences Union.

Abstract

The authors present an approximate analytical model for wind-induced sea-ice drift that includes an ice–ocean boundary layer with an Ekman spiral in the ocean velocity. This model provides an analytically tractable solution that is most applicable to the marginal ice zone, where sea-ice concentration is substantially below 100 %. The model closely reproduces the ice and upper-ocean velocities observed recently by the first ice-tethered profiler equipped with a velocity sensor (ITPV).

The analytical tractability of our model allows efficient calculation of the sea-ice velocity provided that the surface wind field is known and that the ocean surface geostrophic velocity is relatively weak. The model is applied to estimate intraseasonal variations in Arctic sea ice cover due to short-timescale (around 1 week) intensification of the southerly winds. Utilizing 10 m surface winds from ERA-Interim reanalysis, the wind-induced sea-ice velocity and the associated changes in sea-ice concentration are calculated and compared with satellite observations. The analytical model captures the observed reduction of Arctic sea-ice concentration associated with the strengthening of southerlies on intraseasonal time scales. Further analysis indicates that the wind-induced surface Ekman flow in the ocean increases the sea-ice drift speed by 50 % in the Arctic summer. It is proposed that the southerly wind-induced sea-ice drift, enhanced by the ocean's surface Ekman transport, can lead to substantial reduction in sea-ice concentration over a timescale of one week.

1 Introduction

The drift of Arctic sea ice is largely explained by surface winds and upper ocean currents. The effect of the mean geostrophic upper-ocean current on the average circulation of sea-ice pack is known to be as important as the mean wind field (Hibler, 1979; Thorndike and Colony, 1982). However, the role of the winds becomes increasingly important over shorter time scales: on time scales from days to months, surface wind

TCD
9, 2101–2133, 2015

variability explain more than 70 % of the sea-ice motion (Thorndike and Colony, 1982), and is well correlated with the surface ocean velocity (Cole et al., 2014; Kawaguchi and Mitsudera, 2008). The synoptic eddy surface winds result in a primary mode of upper-ocean velocity variability with a period of 2–5 days in the Pacific and Canadian sectors of the Arctic Ocean (Plueddemann et al., 1998). The tight connection between surface winds and upper ocean velocity over ice-covered Arctic Ocean suggests that resolving the eddy wind-induced surface Ekman flow is essential for simulating sea-ice motions.

Many simple sea-ice models assume steady ocean currents and prescribe an empirically-chosen turning angle between ice stress and surface ocean current (Thorndike and Colony, 1982; Bitz et al., 2002; Liu et al., 2011; Uotila et al., 2012). This simple model configuration has limitations in simulating wind-induced sea-ice drift on intraseasonal time scales, during which time-varying Ekman layer flows in the ice–ocean boundary layer (IOBL) may be important. The effect of the surface Ekman flow on sea-ice motion can be resolved by coupling the sea-ice model to a comprehensive ocean model (Zhang and Rothrock, 2003; Uotila et al., 2012). However, such an approach is computationally expensive, and makes it difficult to distinguish the physical processes controlling sea-ice drift. In this study, we derive an approximate analytical solution for wind-induced sea-ice drift that accounts for the Ekman spiral in the IOBL. This analytical model has merits both in theoretical and practical aspects. Because the Ekman layer is resolved in the momentum balance, the turning angle is a prognostic variable in our model. Our model therefore provides an interpretation of recent observations on Arctic sea-ice motions from an ice-tethered profiler (Cole et al., 2014), in particular the angles between the wind and ice velocities and between the ice and ocean velocities. Our treatment of the IOBL is conceptually similar to Rossby similarity theory (McPhee, 1979, 1981, 1994, 2008). We employ a somewhat simpler treatment of the momentum transfer from the sea ice to the IOBL, but it is straightforward to extend our solution to incorporate Rossby similarity theory. The analytical tractability of our model allows efficient calculation of the sea-ice drift, given the surface wind veloc-

TCD
9, 2101–2133, 2015

ity. Moreover, this model allows for an arbitrary mixture of sea ice and water, and is therefore suitable for application to the marginal ice zone.

We use this analytical model to quantify wind-driven intraseasonal variability of sea-ice cover. Many previous observational analyses provided only statistical connections between the southerly winds and sea-ice cover. For example, the strength of south-westerlies over the Barents Sea is well correlated with sea-ice cover in winter (Sorteberg and Kvingedal, 2006; Liptak and Strong, 2013) and the development of anomalous southerlies over the Pacific sector of the Arctic is often followed by a reduction of sea-ice cover in the spring and summer (Wu et al., 2006; Serreze et al., 2003). In this study, we hypothesize that the southerly wind-induced sea-ice advection, accelerated by wind-induced surface Ekman flow, can substantially decrease sea-ice concentration over the course of a week or so. The structure of this paper is as follows. In Sect. 2, we derive an approximate analytical solution for the sea-ice velocity, including an Ekman spiral in the IOBL. In Sect. 3, we describe the data sources and reanalysis products used in this study. In Sect. 4, we validate our model by comparing the analytically-derived wind–ice and ice–ocean velocity angles against recent observations from an ice-tethered profiler. Finally, in Sect. 5 we apply our model to quantify the impact of strong southerly wind events in the Arctic summer on the intraseasonal variability of sea-ice cover.

2 An analytical model for wind-driven sea-ice motion

In this section we employ a simplified sea-ice model to obtain analytical expressions for the sea-ice velocity as a function of surface wind speed. In Sect. 2.1 we formulate an approximate sea-ice momentum balance appropriate for basin-scale motions, and then in Sect. 2.2 we derive an analytical solution for the sea-ice velocity, assuming that the surface wind speed is known.

TCD
9, 2101–2133, 2015

2.1 Model formulation

We employ a "mixture layer" model of Arctic sea ice (Gray and Morland, 1994), which describes the evolution of ice floes interspersed with patches of open water. The thickness-integrated momentum balance for such a mixture layer may be written as (Heorton et al., 2014),

$$\rho_i h_i \frac{D\boldsymbol{u}_i}{Dt} = \varphi\left(\boldsymbol{\tau}_{ai} - \boldsymbol{\tau}_{io}\right) - \rho_i h_i f\left(\hat{\boldsymbol{Z}} \times \boldsymbol{u}_i\right) - \rho_i h_i g \nabla \eta + \nabla \cdot \boldsymbol{\sigma} \tag{1}$$

where h_i is the ice thickness, ρ_i is the ice density, $\boldsymbol{u}_i$ is the ice velocity vector, η is the sea surface height, φ is the sea ice fraction, f is the Coriolis parameter, g is the acceleration due to gravity, and $\hat{\boldsymbol{Z}}$ is a vertical unit vector. Equation (1) states that the ice/water mixture layer is accelerated by momentum exchanges between the ice and the atmosphere ($\boldsymbol{\tau}_{ai}$) and between the ice and the ocean ($\boldsymbol{\tau}_{io}$), by the Coriolis force, by horizontal pressure variations due to sea surface tilt, and by the divergence of a stress tensor ($\boldsymbol{\sigma}$) representing internal friction in the ice.

We first write the lateral pressure gradient term in terms of the ocean near-surface geostrophic velocity $\boldsymbol{u}_g$,

$$f\hat{\boldsymbol{Z}} \times \boldsymbol{u}_g = -\rho_i h_i g \nabla \eta. \tag{2}$$

We are concerned with sea ice evolution over a typical time scale 1 week with a velocity scale of around $0.2\,\mathrm{m\,s^{-1}}$, implying a length scale of around 100 km. The ice acceleration term in Eq. (1) may therefore be safely neglected (McPhee, 1980; Thorndike and Colony, 1982). This precludes the sea ice undergoing inertial oscillations, though the diameter of such oscillations would only be a few km at most, much smaller than the drift length scale of 100 km. In summer, the sea-ice concentration is typically below 80 %, so away from coastal shear margins the internal friction term in Eq. (1) is also negligible (Leppäranta, 2005; Kawaguchi and Mitsudera, 2008). This simplifies the momentum balance to

$$\rho_i h_i f \hat{\boldsymbol{Z}} \times \left(\boldsymbol{u}_i - \boldsymbol{u}_g\right) = \varphi\left(\boldsymbol{\tau}_{ai} - \boldsymbol{\tau}_{io}\right). \tag{3}$$

TCD
9, 2101–2133, 2015

Similar scaling arguments suggest that the pressure gradient due to the sea surface tilt may also be negligible. For now we retain this term because it is analytically tractable, but in Sects. 4 and 5 below, we will neglect the geostrophic ocean velocity term in Eq. (3).

Equation (3) states that the shear between the mixture layer and the ocean's surface geostrophic velocity, or equivalently the total shear across the ice–ocean boundary layer (IOBL; McPhee, 2012) lies perpendicular to the vertical stress divergence in the sea ice. This equation does not account for momentum imparted from the winds to the water between the ice floes in the mixture layer, which we assume to be transferred directly to the ocean below (Gray and Morland, 1994). The total stress felt by the ocean at the base of the mixture layer is therefore

$$\boldsymbol{\tau}_{\mathrm{o}} = (1-\varphi)\boldsymbol{\tau}_{\mathrm{ao}} + \varphi\boldsymbol{\tau}_{\mathrm{io}} \tag{4}$$

where $\boldsymbol{\tau}_{\mathrm{ao}}$ is the momentum imparted to the ocean from the atmosphere between the sea ice floes. We adopt an approach similar to Rossby similarity theory for the IOBL, assuming that the ocean velocity follows an Ekman spiral beneath the mixture layer (McPhee, 2012). The ocean velocity at the top of the Ekman layer is therefore given as

$$\boldsymbol{u}_{\mathrm{o}} - \boldsymbol{u}_{\mathrm{g}} = \frac{1}{\sqrt{2K_{\mathrm{o}}^{*}}}\left(\boldsymbol{u}_{\mathrm{o}}^{*} - \hat{Z}\times\boldsymbol{u}_{\mathrm{o}}^{*}\right) \tag{5}$$

where $K_{\mathrm{o}}^{*} = Kf/|\boldsymbol{u}_{\mathrm{o}}^{*}|^{2}$ is the dimensionless vertical eddy diffusivity, K is the dimensional vertical eddy diffusivity, $\boldsymbol{u}_{\mathrm{o}}^{*}$ is a stress velocity defined by $\boldsymbol{\tau}_{\mathrm{o}} = \rho_{\mathrm{o}}|\boldsymbol{u}_{\mathrm{o}}^{*}|\boldsymbol{u}_{\mathrm{o}}^{*}$, and ρ_{o} is the ocean surface density. The dimensionless diffusivity K_{o}^{*} is taken to be constant, reflecting a linear dependence of the Ekman layer depth on the stress velocity. This is appropriate for IOBLs with no surface buoyancy forcing; non-zero surface buoyancy modifies the vertical profile of K in the IOBL (McPhee, 2008). Our model could be extended to accommodate an arbitrary K-profile if the surface buoyancy fluxes were known, but for simplicity in this study we assume zero surface buoyancy forcing.

TCD
9, 2101–2133, 2015

We prescribe the air–ice, air–ocean, and ice–ocean stresses using quadratic drag relations,

$$\boldsymbol{\tau}_{ai} = \rho_a C_{ai} |\boldsymbol{u}_a| \boldsymbol{u}_a = \rho_a \left| \boldsymbol{u}^*_{ai} \right| \boldsymbol{u}^*_{ai} \tag{6a}$$

$$\boldsymbol{\tau}_{ao} = \rho_a C_{ao} |\boldsymbol{u}_a| \boldsymbol{u}_a = \rho_a |\boldsymbol{u}^*_{ao}| \boldsymbol{u}^*_{ao} \tag{6b}$$

$$\boldsymbol{\tau}_{io} = \rho_o C_{io} |\boldsymbol{u}_i - \boldsymbol{u}_o| (\boldsymbol{u}_i - \boldsymbol{u}_o) = \rho_o \left| \boldsymbol{u}^*_{io} \right| \boldsymbol{u}^*_{io} \tag{6c}$$

where ρ_a and ρ_o are the atmospheric and surface ocean density respectively. Here we have implicitly assumed that there exists thin turbulent boundary layers between the atmosphere and the ice floes, between the atmosphere and ocean leads, and between the bases of the ice floes and the top of the Ekman layer, all of which transfer momentum at a rate that varies quadratically with the vertical shear. We have further assumed that any momentum imparted to the ocean leads is transferred directly down to the Ekman layer below. More comprehensive treatments of the ice–ocean stress may be derived using Rossby similarity theory (McPhee, 2008, 2012). However, application of this theory becomes complicated by the presence of leads between the sea ice floes, which continually change the surface boundary condition at any given point between a free surface and a rigid ice floe. In many previous studies, these stresses carry a turning angle to account for the effect of the Coriolis force in the boundary layer (Hibler, 1979; Thorndike and Colony, 1982; Bitz et al., 2002; Uotila et al., 2012). This is not necessary here because we use the ageostrophic 10 m winds, and we explicitly account for the ocean surface Ekman layer.

By combining the ice–ocean stress relation Eq. (6c), which can be rewritten as $\boldsymbol{u}^*_{io} = \sqrt{C_{io}}(\boldsymbol{u}_i - \boldsymbol{u}_o)$, with Eq. (5) for the shear across the Ekman layer, we obtain an expression for the total shear across the IOBL,

$$\boldsymbol{u}_i - \boldsymbol{u}_g = \frac{1}{\sqrt{C_{io}}} \boldsymbol{u}^*_{io} + \frac{1}{\sqrt{2K^*_0}} \left(\boldsymbol{u}^*_o - \hat{Z} \times \boldsymbol{u}^*_o \right). \tag{7}$$

TCD
9, 2101–2133, 2015

Then, substituting Eqs. (6a), (6c) and (7) into the momentum balance Eq. (3), we obtain a relationship between the unknown stress velocities $\boldsymbol{u}^*_{io}$ and $\boldsymbol{u}^*_{o}$,

$$\frac{\rho_i h_i f}{\sqrt{C_{io}}}\hat{Z}\times\boldsymbol{u}^*_{io}+\frac{\rho_i h_i f}{\sqrt{2K^*_0}}\left(\hat{Z}\times\boldsymbol{u}^*_{o}+\boldsymbol{u}^*_{o}\right)=\varphi\left(\rho_a\left|\boldsymbol{u}^*_{ai}\right|\boldsymbol{u}^*_{ai}-\rho_o\left|\boldsymbol{u}^*_{io}\right|\boldsymbol{u}^*_{io}\right). \tag{8}$$

We require an additional equation to obtain an explicit solution for $\boldsymbol{u}^*_{io}$ and $\boldsymbol{u}^*_{o}$, so we rewrite the total stress at the base of the mixing layer Eq. (4) in the form

$$\rho_o|\boldsymbol{u}^*_{o}|\boldsymbol{u}^*_{o}=(1-\varphi)\rho_a|\boldsymbol{u}^*_{ao}|\boldsymbol{u}^*_{ao}+\varphi\rho_o\left|\boldsymbol{u}^*_{io}\right|\boldsymbol{u}^*_{io}. \tag{9}$$

2.2 Model solution

We now solve Eqs. (8) and (9), derived in the previous subsection, analytically for the stress velocities $\boldsymbol{u}^*_{io}$ and $\boldsymbol{u}^*_{o}$, and thus for the ice velocity $\boldsymbol{u}_i$. In this subsection we focus on the simplest case of 100 % sea ice cover ($\varphi = 1$). In this case the method of solution is very similar to that described by Leppäranta (2005, Chapt. 6.1), but our explicit treatment of the oceanic boundary layer and prognostic determination of the turning angle warrant that the solution be given in full. In the Appendix we discuss the solution for the general case of partial sea ice cover ($\varphi \le 1$), which is more complicated. For $\varphi = 1$, Eq. (9) simplifies to $\boldsymbol{u}^*_{io} = \boldsymbol{u}^*_{o}$, and thus Eqs. (7) and (8) may be rewritten as

$$\boldsymbol{u}_i-\boldsymbol{u}_g=\left(\frac{1}{\sqrt{C_{io}}}+\frac{1}{\sqrt{2K^*_0}}\right)\boldsymbol{u}^*_{io}-\frac{1}{\sqrt{2K^*_0}}\hat{Z}\times\boldsymbol{u}^*_{io} \tag{10a}$$

$$\left(\frac{\rho_i h_i f}{\sqrt{2K^*_0}}+\frac{\rho_i h_i f}{\sqrt{C_{io}}}\right)\hat{Z}\times\boldsymbol{u}^*_{io}+\frac{\rho_i h_i f}{\sqrt{2K^*_0}}\boldsymbol{u}^*_{io}=\rho_a\left|\boldsymbol{u}^*_{ai}\right|\boldsymbol{u}^*_{ai}-\rho_o\left|\boldsymbol{u}^*_{io}\right|\boldsymbol{u}^*_{io}. \tag{10b}$$

TCD
9, 2101–2133, 2015

We simplify the coefficients by multiplying both sides of Eq. (10b) by $\sqrt{2K_0^*/\rho_i h_i f}$ and rearranging to obtain

$$(\alpha+1)\hat{Z}\times\boldsymbol{u}_{io}^* + \left(1+k_o\left|\boldsymbol{u}_{io}^*\right|\right)\boldsymbol{u}_{io}^* = k_a\left|\boldsymbol{u}_{ai}^*\right|\boldsymbol{u}_{ai}^* \tag{11}$$

where

$$\alpha=\sqrt{2K_0^*/C_{io}},\ k_a=\rho_a\sqrt{2K_0^*/\rho_i h_i f} \text{ and } k_o=\rho_o\sqrt{2K_0^*/\rho_i h_i f}. \tag{12}$$

To solve, we first define the components of $\boldsymbol{u}_{io}^*$ parallel and perpendicular to the wind stress velocity, or, equivalently, perpendicular the 10 m winds:

$$u_{io}^{*\parallel} = \frac{\boldsymbol{u}_{ai}^*}{\left|\boldsymbol{u}_{ai}^*\right|}\cdot\boldsymbol{u}_{io}^* \tag{13a}$$

$$u_{io}^{*\perp} = \left(\hat{Z}\times\frac{\boldsymbol{u}_{ai}^*}{\left|\boldsymbol{u}_{ai}^*\right|}\right)\cdot\boldsymbol{u}_{io}^*. \tag{13b}$$

Then taking the dot product of $\boldsymbol{u}_{io}^*$ with both sides of Eq. (11) and rearranging yields an expression for $u_{io}^{*\parallel}$,

$$u_{io}^{*\parallel} = \frac{1}{k_a}\frac{\left|\boldsymbol{u}_{io}^*\right|^2}{\left|\boldsymbol{u}_{ai}^*\right|^2}\left(1+k_o\left|\boldsymbol{u}_{io}^*\right|\right) \tag{14}$$

while taking the dot product of $\hat{Z}\times\boldsymbol{u}_{io}^*$ with both sides of Eq. (11) yields an expression for $u_{io}^{*\perp}$,

$$u_{io}^{*\perp} = -\frac{1}{k_a}\frac{\left|\boldsymbol{u}_{io}^*\right|^2}{\left|\boldsymbol{u}_{ai}^*\right|^2}(1+\alpha). \tag{15}$$

TCD
9, 2101–2133, 2015

Equations (14) and (15) do not constitute an explicit solution for $\boldsymbol{u}^*_{\mathrm{io}}$ because they depend on the magnitude $\left|\boldsymbol{u}^*_{\mathrm{io}}\right|$. We determine this magnitude using the definition, $\left|\boldsymbol{u}^*_{\mathrm{io}}\right|^2 = \left(u^{*\parallel}_{\mathrm{io}}\right)^2 + \left(u^{*\perp}_{\mathrm{io}}\right)^2$, which yields a quartic equation for $\left|\boldsymbol{u}^*_{\mathrm{io}}\right|$,

$$k_{\mathrm{o}}^2 \left|\boldsymbol{u}^*_{\mathrm{io}}\right|^4 + 2k_{\mathrm{o}} \left|\boldsymbol{u}^*_{\mathrm{io}}\right|^3 + \left(1 + (\alpha+1)^2\right) \left|\boldsymbol{u}^*_{\mathrm{io}}\right|^2 = k_{\mathrm{a}}^2 \left|\boldsymbol{u}^*_{\mathrm{ai}}\right|^4. \tag{16}$$

In principle, this may be solved analytically for $\left|\boldsymbol{u}^*_{\mathrm{io}}\right|$, but for the purposes of this study we solve Eq. (11) numerically. Note that the right-hand side of Eq. (11) is a monotonically increasing function of $\left|\boldsymbol{u}^*_{\mathrm{io}}\right|$, so a unique solution exists for any wind stress velocity $\left|\boldsymbol{u}^*_{\mathrm{ai}}\right|$. Having obtained the components of the stress velocity, it is straightforward to solve for the shear between the sea ice and the geostrophic ocean velocity using Eq. (10a).

Though Eqs. (14)–(16) constitute an analytical solution to the mixture layer momentum balance Eq. (11), in this form they yield little insight into the wind-driven drift of sea ice. We therefore provide additional formulae for some key quantities describing the ice drift. The IOBL turning angle, being the angle between the ice–ocean stress velocity $\boldsymbol{u}^*_{\mathrm{io}}$ and the ice-geostrophic shear $(\boldsymbol{u}_{\mathrm{i}} - \boldsymbol{u}_{\mathrm{g}})$, may be derived by taking the dot product of Eq. (10a) with $\boldsymbol{u}^*_{\mathrm{io}}$:

$$\cos\left(\theta_{\mathrm{IOBL}}\right) = \frac{1+\alpha}{\sqrt{1+(1+\alpha)^2}}. \tag{17}$$

Thus, the IOBL turning angle is independent of the surface wind speed for 100 % sea ice concentration. Equations (5) and (6c), prescribing an Ekman spiral and a linear relationship between the ice–ocean stress velocity $\boldsymbol{u}^*_{\mathrm{io}}$ and the ice–ocean shear $(\boldsymbol{u}_{\mathrm{i}} - \boldsymbol{u}_{\mathrm{o}})$, are equivalent to assuming a constant geostrophic ice–ocean turning angle (e.g. Hibler, 1979; Thorndike and Colony, 1982). In reality θ_{IOBL} depends on the ice–ocean stress $\boldsymbol{u}^*_{\mathrm{io}}$, but the turning angle varies by only a few degrees over a realistic range of ice–ocean stress magnitudes (McPhee, 1979, 2008). Note that in our model θ_{IOBL} is

TCD
9, 2101–2133, 2015

generally not independent of the surface wind speed when the sea ice concentration is below 100 %.

We now turn to the ice drift itself. We derive the angle between the 10 m wind speed $\boldsymbol{u}_a$ and the ice-geostrophic shear $\boldsymbol{u}_i - \boldsymbol{u}_g$ by taking the dot product of $\boldsymbol{u}^*_{ai}$ with Eq. (10a), noting that $\boldsymbol{u}^*_{ai}$ lies parallel to $\boldsymbol{u}_a$ from Eq. (6a), and using Eqs. (14) and (15) for the components of $\boldsymbol{u}^*_{io}$,

$$\cos(\theta_{ai}) = \frac{k_o \left|\boldsymbol{u}^*_{io}\right|^2}{k_a \left|\boldsymbol{u}^*_{ai}\right|^2} \frac{1+\alpha}{\sqrt{1+(1+\alpha)^2}} = \frac{|\boldsymbol{\tau}_{io}|}{|\boldsymbol{\tau}_{ai}|} \cos(\theta_{IOBL}). \tag{18}$$

Using Eq. (16) above, it is straightforward to show that the ratio of the ice–ocean to air–ice stresses is smaller than one, $k_o \left|\boldsymbol{u}^*_{io}\right|^2 / k_a \left|\boldsymbol{u}^*_{ai}\right|^2 = |\boldsymbol{\tau}_{io}| / |\boldsymbol{\tau}_{ai}| < 1$, so it follows that the air–ice angle is always at least as large as the IOBL turning angle, $\theta_{ai} \geq \theta_{IOBL}$. This reflects the fact that the 10 m wind velocity $\boldsymbol{u}_a$ always points to the left of the ice–ocean stress $\boldsymbol{\tau}_{io}$ (cf. Eqs. 14 and 15), while the ice–geostrophic shear $\boldsymbol{u}_i - \boldsymbol{u}_g$ always points to the right of $\boldsymbol{\tau}_{io}$ (cf. Eq. 10a). For strong winds ($|\boldsymbol{\tau}_{ai}| \to \infty$) Eq. (16) implies that the air–ice and ice–ocean stresses balance one another in Eq. (3) (i.e. $\boldsymbol{\tau}_{io} \to \boldsymbol{\tau}_{ai}$), so the air–ice turning angle becomes independent of the wind speed and equal to the IOBL turning angle. For weak winds ($|\boldsymbol{\tau}_{ai}| \to 0$) Eq. (16) implies that the ice–ocean to air–ice stress ratio vanishes, $|\boldsymbol{\tau}_{io}| / |\boldsymbol{\tau}_{ai}| \to 0$, so from Eq. (18) the ice velocity becomes directed 90° to the right of the winds.

3 Observation and reanalysis datasets

In this section we detail the various observational and reanalysis datasets used to validate our analytical model and to quantify how southerly winds affects Arctic summer sea-ice concentration.

TCD
9, 2101–2133, 2015

3.1 Observations

To validate our analytical model with observations, we used observations from an ice-tethered profiler (ITP; Toole et al., 2010) equipped with a velocity sensor (ITP-V; Williams et al., 2010). Specifically, we use data from ITP-V 35, which was deployed on 8 October 2009 on an ice floe in the Beaufort Sea at 77° N, 135° W, as part of the Beaufort Gyre Observing System (BGOS). The ice floe was 2.6 m thick, so hydrostatic adjustment resulted in an ice–ocean interface at around 2.3 m depth (Cole et al., 2014). Ocean velocity profiles were obtained every 4 h to 150 m depth, with an effective vertical resolution of 1 m. To examine the ice–ocean shear ($\boldsymbol{u}_\mathrm{i} - \boldsymbol{u}_\mathrm{o}$) and the ice–ocean velocity angle, we use the shallowest consistently-available measurements from the velocity profiles, at a depth of 7 m. The ice velocity ($\boldsymbol{u}_\mathrm{i}$) is derived from hourly GPS fixes and linearly interpolated in time to align with the time of the ITP-V 35 observations. Further details, including calibrations and a discussion of errors in ITP-V 35, are described by Cole et al. (2014).

Arctic sea-ice concentration data is from the US National Snow and Ice Data Center (NSIDC), and is based on satellite-derived passive microwave brightness temperature. Specifically, the NASA Team Algorithm (Swift and Cavalieri, 1985) was used to estimate the sea-ice concentration. These data are provided as a daily mean on a polar stereographic grid with 25 km × 25 km resolution. We re-gridded this data onto a regular 1.0° × 1.0° grid.

3.2 Reanalysis

Observations of Arctic sea-ice thickness are sparse, so instead we use the coupled Pan-Arctic Ice–Ocean Modeling and Assimilation System (PIOMAS; Zhang and Rothrock, 2003) to estimate the basin scale Arctic sea-ice thickness. PIOMAS consists of a 12-category thickness and enthalpy distribution sea ice model coupled with the POP (Parallel Ocean Program) ocean model (Smith et al., 1992). The data is monthly and covers from the year 1978 to 2013. For atmospheric winds, we used 10 m winds

TCD
9, 2101–2133, 2015

provided by the European Center for Medium-Range Weather Forecasts ERA-Interim reanalysis dataset (Dee et al., 2011). The data is 6 hourly with a horizontal resolution of 1.0° × 1.0°.

4 Analytical model validation

In this section, we validate our analytical model against the ITP-V 35 observations of sub-sea ice ocean velocity. Specifically, we examine whether the modeled wind–ice and ice–ocean velocity angles are consistent with the observations.

4.1 Model parameters

The ITP-V 35 was deployed upon a 2.6 m-thick ice floe, which is much thicker than the mean ice thickness over the western Beaufort Sea. Figure 1a shows the PIOMAS sea-ice thickness averaged from October 2009 to March 2010. During this time period, sea-ice thickness over the western Beaufort Sea (around 74–78° N, 135–150° W) is around 1.4–1.6 m. It is therefore likely that ITP-V 35 was mounted on a relatively sturdy floe, whereas much of the surrounding floes were a lot thinner. The velocity of the mixture layer (see Sect. 2) represents a bulk average over many floes, and similarly the ocean Ekman layer in any given location responds to stresses transmitted by a series of ice floes passing overhead. For the purpose of model validation we therefore take the sea-ice thickness h_i to be 1.5 m, which is appropriate for basin-scale sea-ice momentum balance. For simplicity and for comparison with Rossby similarity theory, we assume 100 % sea-ice cover ($\varphi = 1$). This is reasonable because the mean sea-ice concentration over the western Beaufort Sea is mostly over 85–90 % from October to March (Fig. 1b).

Observational fits to suggest that the annual mean value of the dimensionless vertical eddy diffusivity K_0^* is about 0.028 (McPhee, 1994, 2008). However, our treatment of the IOBL in Sect. 2 is formally only applicable to neutrally-stratified boundary lay-

TCD
9, 2101–2133, 2015

ers with no surface buoyancy flux. The ITP-V observations mostly cover winter season (from October to March), when surface buoyancy loss due to sea ice formation enhances the vertical eddy diffusivity by a factor of up to 10 (McPhee and Morison, 2001). Below we therefore test our model using the canonical value of $K_0^* = 0.028$ and an enhanced value of $K_0^* = 0.1$; the former and the latter values might be suitable for the annual mean and winter respectively. Finally, the geostrophic current in the interior of polar oceans, $\boldsymbol{u}_g$, is poorly constrained, and we assume that this term is small relative to the surface current. This assumption should be more robust on intraseasonal time scales, as surface winds can strengthen rapidly in a few days, so the resultant surface Ekman velocity is likely to be much larger than the interior geostrophic flow.

For other parameters, we used standard values used in many previous studies: $\rho_a = 1.35\,\mathrm{kg\,m^{-3}}$, $\rho_i = 910\,\mathrm{kg\,m^{-3}}$, and $\rho_o = 1000\,\mathrm{kg\,m^{-3}}$. The atmospheric drag coefficients C_{ai} and C_{ao} depend on the season, the ice fraction, and the surface roughness (Lüpkes et al., 2012), but for simplicity we use a constant values of $C_{ai} = 1.89 \times 10^{-3}$ and $C_{ai} = 1.25 \times 10^{-3}$ (Lüpkes and Birnbaum, 2005). We prescribe the ice–ocean drag coefficient C_{io} based on the findings of Cole et al. (2014), who found that $C_{io} = 7.1 \times 10^{-3}$ best fit the ITP-V 35 measurements.

4.2 Results

Figure 2 shows the observed ice speed (black line) as a function of the 10 m wind speed. Consistent with Thorndike and Colony (1982), the relationship is linear, except for weak winds (speed less than $2\,\mathrm{m\,s^{-1}}$). For moderately strong winds, sea-ice moves with a speed around 1.5–2 % of the surface wind speed. This is consistent or slightly weaker than an old rule-of-thumb that suggests 2 % relationship (Thorndike and Colony, 1982). It may be that sea ice formation, and thus surface buoyancy loss, leads to stronger mixing (larger K_0^*) in the IOBL, which reduces the sea ice speed (see Fig. 2). The internal stresses in the relatively concentrated sea ice (85–90 % in winter) may also impede sea ice motion. In general, our analytical model (red and blue lines)

TCD
9, 2101–2133, 2015

predicts this relationship quite well, though only the solution with strong vertical diffusivity ($K_o^* = 0.1$) is within the error bars. As introduced, ITP-V 35 was deployed mostly during winter, so larger vertical diffusivity (blue-dotted line; $K_o^* = 0.1$) fits better with the observations. Using the canonical value of $K_o^* = 0.028$ overestimates the ice speed by 30–50 %.

Figure 3a shows that the wind–ice velocity angle θ_{ai} decreases as the surface wind strengthens, consistent with previous observations (Thorndike and Colony, 1982). The analytical model with $K_o^* = 0.1$ reproduces this curve remarkably well. The velocity angle is overestimated by 5–10° in the case when the canonical vertical diffusivity $K_o^* = 0.028$ is used. From Eq. (18), θ_{ai} is proportional to the ratio between the ice–ocean stress and wind–ice stress ($\theta_{ai} \propto |\boldsymbol{\tau}_{io}|/|\boldsymbol{\tau}_{ai}|$). Thus, the decrease of θ_{ai} with increasing surface wind speed indicates that the stress ratio, $|\boldsymbol{\tau}_{io}|/|\boldsymbol{\tau}_{ai}|$ increases as surface wind strengthens. In other words, the momentum becomes more effectively transferred down to the ocean as the surface wind speed increases. For relatively weak winds, the observational errors in θ_{ai} (gray shadings in Fig. 3a) are large, whereas for stronger winds the air–ice velocity angle is much better constrained (Cole et al., 2014).

The shallowest measurement depth of ITP-V 35 is 7 m, and the Ekman spiral rotates the velocity quite substantially between the ice base (~ 2.6 m) and 7 m. Consequently the ITPV data is not suitable for estimating the IOBL turning angle. Instead we test our analytical treatment of the IOBL using the velocity angle between the ice floe and the ocean at 7 m $\theta_{io}|_{z=-7m}$ as a function of ice speed, shown in Fig. 3b. In general, the ice–ocean velocity angle $\theta_{io}|_{z=-7m}$ decreases as ice speed increases. Consistent with Cole et al. (2014), the errors in $\theta_{io}|_{z=-7m}$ are quite large, especially for low ice speeds. To calculate $\theta_{io}|_{z=-7m}$ from the analytical model, the velocity angle needs to be adjusted by the Ekman layer solution, which can be presented as a function of ocean depth, z:

$$\boldsymbol{u}(z) = \boldsymbol{u}_o \exp\left(\frac{z + h_o}{\delta_E}\right) \exp\left(i\frac{z + h_o}{\delta_E}\right). \quad (19)$$

TCD
9, 2101–2133, 2015

Here $\boldsymbol{u}_o$ is the ocean surface velocity at the bottom of sea ice, $h_o = (\rho_i/\rho_o)h_i$ is the depth of the ice base, and $\delta_E = \sqrt{2K}/f$ is the Ekman depth. We have used complex variables to describe two-dimensional vectors, e.g. $\boldsymbol{u}_o = (u_o, v_o) \equiv u_o + iv_o$, because this presents changes in vector orientation more intuitively. The complex term, $\exp\left(i(z+h_o)/\delta_E\right)$, produces a velocity $\boldsymbol{u}|_{z=-d}$ at any depth d that is rotated relative to $\boldsymbol{u}_o$ by a clockwise angle of $(d-h_o)/\delta_E$ radians. Thus the adjusted velocity angle between the ice and the ocean at any depth in the Ekman layer is:

$$\theta_{io}|_{z=-d} = \theta_{io}|_{z=-h_o} + (d-h_o)/\delta_E. \quad (20)$$

Our analytical solution for the ice–ocean velocity angle, adjusted using Eq. (20), agrees reasonably well with the ITP-V 35 measurements. Again, the analytical model predicts the observational curve better when the higher vertical diffusivity of $K_o^* = 0.1$ is used. In summary, the analytical model estimates the observed wind–ice and ice–ocean velocity angles well: for $K_o^* = 0.1$ the model prediction almost always lies within the observational eror bars, indicating that the model captures the essential dynamics of the wind-induced sea-ice motions.

As briefly mentioned, our analytically tractable solution provides several merits in calculating sea-ice motions. First, this model derives equations for the mixture of sea ice and water ($\varphi \ll 1$), which is suitable for marginal ice zone. Second, this model describes sea-ice motion as a function of ice thickness h_i. In Fig. 4 we plot the sensitivity of the wind–ice velocity angle (θ_{ai}) and the IOBL turning angle (θ_{IOBL}) to a range of sea-ice concentrations (φ) and ice thicknesses (h_i). In general, the wind–ice velocity angle increases substantially with sea ice thickness (Fig. 4a): for a moderate wind speed of $6\,m\,s^{-1}$, increasing the sea ice thickness from 0.25 to 3 m increases this angle from 20 to 60°. By contrast, for 100 % sea-ice concentration the IOBL turning angle is independent of the ice thickness (Fig. 4c). It can be inferred from Eq. (18) that *thicker* ice is *less efficient* in transferring the momentum into the ocean, leading to larger wind–ice velocity angle; thicker ice absorbs more of the wind-input momentum into the Coriolis torque, transmitting less to the ocean below.

TCD
9, 2101–2133, 2015

Sea-ice concentration also strongly influences these angles. Figure 4b shows that wind–ice velocity angle increases as sea-ice concentration decreases. There is little difference in this angle between 100 and 75 % ice concentrations – the angle is less sensitive at relatively high sea-ice concentrations. However, the angle rapidly increases as sea-ice concentration gets below 50 %: at 25 % sea ice concentration the wind–ice angle is 20° larger than at 100 % concentration, even for the strongest winds in the dataset. The response of IOBL turning angle to the mixture of sea ice and water ($\varphi \ll 1$) is rather surprising (Fig. 4d). The turning angle is negative for weaker surface winds in the case when sea-ice concentration is less than 100 %. This is because wind stress over the ice-free component of the mixture layer is transmitted directly to the water below. As the sea ice concentration approaches zero, the stress transmitted through the ice becomes negligible in determining the direction of the surface Ekman velocity ($\boldsymbol{u}_o$). Because the ITP-V 35 track covers mostly ice-covered regions ($\varphi \approx 1$) and the shallowest measurement depth is 7 m, it is difficult to verify whether negative IOBL turning angles appear in the observations.

5 Application to wind-driven summer sea ice changes

In this section, we quantify the effect of southerly winds on Arctic sea ice cover using near-surface wind data, and compare the results with satellite observations. There are several notable Arctic weather perturbations in the spring and summer over the Pacific sector of the Arctic Ocean, such as the development of the Arctic dipole mode (Wu et al., 2006), quasi-stationary cyclonic winds (Serreze et al., 2003) and synoptic cyclones (Zhang et al., 2013). These perturbations are often accompanied by rapid strengthening of southerlies and a reduction of the sea ice concentration (SIC) on intraseasonal time scales. In the Arctic summer, sea-ice thickness is mostly below 2 m (Fig. 5a) and the area of the marginal ice zone with a moderate SIC (25–75 %) is quite large (Fig. 5b). We therefore hypothesize that the strengthening of southerlies should efficiently redistribute the sea-ice cover in the summer.

TCD
9, 2101–2133, 2015

5.1 Methods

For surface wind forcing, we used the ERA-Interim reanalysis. Arctic sea-ice concentration data is from the US National Snow and Ice Data Center (NSIDC). The Arctic sea-ice concentration shows multi-decadal declining trend which was removed for each calendar day and for each grid. For sea-ice thickness, we used the climatological mean PIOMAS sea-ice thickness data averaged from 1990 to 2012.

Using the analytical solutions derived in Sect. 2, sea-ice velocity is calculated from the ERA-Interim daily 10 m winds. Then, lagged composite analyses are performed in order to investigate how a rapid development of southerlies affects sea-ice concentration during the Arctic summer. We used data from 1990 to 2012 and focused on the summer, from 1 August to 30 September (AS). To define the events of the rapid strengthening of southerlies, the surface winds over the Pacific sector of the Arctic are zonally and meridionally averaged, from 150 to 230° E and from 70 to 90° N (cosine weighting is applied to each latitude). Then, the southerly wind event is defined as a time period when the averaged southerly wind value exceeds 1 SD for three or more consecutive days. If the beginning of an event occurs within 7 days of the end of the preceding event, then the latter event is discarded. This procedure identifies 27 events during the analysis period. Lag zero is defined as the day when the averaged southerly winds peak. Prior to generating the composites, a 3 day moving average is applied to filter out noise associated with day-to-day fluctuations.

These southerly wind-induced sea-ice drifts redistribute sea-ice concentration. This effect is computed using the following evolution equation: $\mathrm{d}I_c = -\left[\frac{\partial(U_i I_c)}{\partial x} + \frac{\partial(V_i I_c)}{\partial y}\right]\Delta t$. Here I_c is sea-ice concentration, which ranges from 0 to 1, at each grid point, and Δt is a time step, which has a length of one day in this study. To calculate sea ice concentration anomalies we subtract the long-term climatological mean $\mathrm{d}I_c$ from the daily $\mathrm{d}I_c$ during the southerly wind events. Then, the anomalous daily $\mathrm{d}I_c$ is integrated from the lag day −8 to estimate the cumulative changes in sea-ice concentration associated with the southerly wind events:

TCD
9, 2101–2133, 2015

$$\Delta I_c = -\sum_{t=-8}^{t=\mathrm{lag}} \left[\frac{\partial (U_i I_c)}{\partial x} + \frac{\partial (V_i I_c)}{\partial y} \right]' \Delta t. \quad (21)$$

Here, prime $()'$ denotes a deviation from the long-term climatological mean. The time integration starts from the lag –8 because the southerly wind events, on average, start about a week before they peak. The results we present are not very sensitive to the starting date. The maximum and the minimum limit of the cumulative changes in sea-ice concentration (ΔI_c) is constrained by the mean sea-ice concentration, which is between 0 and 100 %. For example, if the cumulative changes in the mean sea-ice concentration ($\Delta I_c + \overline{I_c}$), where $\overline{I_c}$ is the climatological mean sea-ice concentration, is above 100 %, then ΔI_c is given as $(100 - \overline{I_c})$%. All of the analytical model results presented here use a dimensionless vertical diffusivity of $K_o^* = 0.028$ (McPhee, 2011).

5.2 Results

Figure 6 illustrates the response of the SIC (shadings in the left column) to the development of southerlies (vectors in the left column) from the East Siberian and Chukchi Sea. Over a 10 day period, the SIC in these regions decreases by 7–8 %. The relative timing suggests that the reduction of SIC is caused by the southerly wind-induced sea-ice drift. To further test this possibility, the wind-induced redistribution of SIC is calculated using our model, specifically Eqs. (A1a–b; see Appendix). The result, shown in the right column of Fig. 1, captures the spatial pattern in the observed SIC anomalies. The anomalous sea-ice velocity (vectors in the right column) is generally directed towards the Beaufort Sea, a little east of the surface wind velocity with the drift angle raging between 20 and 45°. The calculated SIC anomalies at day +6 (bottom row of Fig. 6) are largely consistent with the satellite observed SIC anomalies. However, the calculated SIC anomalies somewhat underestimate the observation. At day +6, the calculated reduction of SIC over the Pacific sector is about 4–5 %, whereas the observed reduction

TCD
9, 2101–2133, 2015

of SIC is up to 6–7 %. There are several factors affecting our calculations. It is possible that the real sea-ice thickness in the Arctic summer is thinner than the PIOMAS sea-ice thickness. Or, the vertical diffusivity K_0^* in August and September might be smaller than 0.028 due to surface buoyancy input resulting from sea ice melt (McPhee and Morison, 2001).

Finally, we ask: to what extent does the IOBL modulate the sea-ice velocity? We have neglected the ocean surface geostrophic velocity in our analytical model calculations, retaining only the surface Ekman layer. However, if the Ekman layer velocity were sufficiently weak compared to the ice velocity then we could simply neglect the ocean velocity altogether. In Fig. 7 we compare the sea ice speed anomalies with and without an IOBL included in the model. Both curves have been generated by averaging the sea ice speed anomalies over the Pacific sector of the Arctic (from 150 to 230° E and from 70 to 90° N), and then calculating lagged composites across all southerly wind events. This plot illustrates that the IOBL enhances the wind-induced sea-ice speed by 50 %. We therefore conclude that acceleration of the sea ice speed by the IOBL plays a substantial role in the rapid reduction of SIC associated with strong southerly wind events.

6 Summary and discussion

In this study we have derived an analytical model for wind-induced sea-ice drift, validated our model against measurements from a velocity sensor-equipped ice-tethered profiler (ITP-V), and used the model to demonstrate that Arctic southerly wind events drive substantial reductions in sea ice concentration over short timescales. Our model is conceptually similar to Rossby similarity theory (McPhee, 2008) for the ice–ocean boundary layer (IOBL). The key features of this model are:

1. The ice floes and leads containing open water are described via a bulk "mixture layer", momentum balance, following Gray and Morland (1994).

TCD
9, 2101–2133, 2015

2. The IOBL consists of an Ekman layer whose depth is assumed to depend linearly on the surface stress velocity (McPhee, 2011), most appropriate for a neutrally stratified IOBL with no surface buoyancy flux (McPhee and Morison, 2001).

3. The transfer of momentum between the 10 m winds, the ice and ocean components of the mixture layer, and the ocean surface layer are assumed to follow a quadratic drag laws. By contrast Rossby similarity theory assumes the "law of wall" to hold in a narrow boundary layer at the top of the IOBL (McPhee, 2008).

Though the simplicity of our model carries several caveats, discussed below, it also confers several advantages. For example, the analytical tractability of the model makes it very efficient, certainly much more so than running a full coupled model of the Arctic. This makes the model straightforward to interpret; the analytical expressions in Sect. 2 yield physical insight into the velocity observations from ITP-V 35 and the sea ice concentration data from NSIDC. The model's "mixture layer" formulation (Gray and Morland, 1994) also makes it suitable for the marginal ice zone.

Our analytical approach was possible because we assumed a constant vertical diffusivity in the surface Ekman layer. This simplification results in an IOBL turning angle (θ_{IOBL}) that is independent of ice–ocean stress $\boldsymbol{u}^*_{\mathrm{io}}$ in our model, whereas the turning angle slightly decreases as the ice–ocean stress strengthens in observations (McPhee, 2008). It would be straightforward to extend our model to incorporate Rossby similarity theory and a stratified IOBL, assuming that some means of parameterizing the surface buoyancy flux were available. Importantly, we also neglected internal stresses in the ice, which can feature prominently in the momentum balance when the sea ice concentration is close to 100 % (Leppäranta, 2005). Nonetheless, the wind–ice and ice–ocean velocity angles predicted by our analytical model match well with the recent ITP-V 35 observations. This agreement improves if we use a larger IOBL vertical diffusivity, which we speculate is either due to stronger turbulent mixing due to surface buoyancy loss, or due to impedance of the sea-ice motion by internal stress.

TCD
9, 2101–2133, 2015

We applied our analytical model to investigate the strong southerly events in the Arctic summer to estimate the wind-induced reduction of SIC. The calculated reduction of SIC is largely consistent with satellite observations, although the reduction rate is somewhat underestimated. Our results verify that the southerly wind-induced sea-ice drift can substantially decrease SIC in a week. Because the wind-induced sea-ice drift can be directly calculated from our analytical solution, the underlying processes for the sea-ice variability might be better identified by utilizing reanalysis data. We suggest that our analytical model can be a flexible tool for identifying and quantifying the mechanisms for the Arctic and Antarctic sea-ice cover variability, which is often associated with the changes in the global-scale circulation pattern (Lee et al., 2011; Holland and Kwok, 2012; Bitz and Polvani, 2012; Li et al., 2014; Wettstein and Deser, 2014; Raphael and Hobbs, 2014).

Appendix

In this appendix we discuss the solution of our model, described in Sect. 2.1, for sea ice concentrations below 100 % ($\varphi \le 1$). We begin by simplifying the coefficients in Eqs. (8) and (9) by defining α, k_a, and k_o as in Sect. 2.1, and additionally defining $\beta = \rho_a C_{ao}/\rho_o C_{ai}$,

$$\alpha \hat{Z} \times \boldsymbol{u}^*_{io} + \hat{Z} \times \boldsymbol{u}^*_{o} + \boldsymbol{u}^*_{o} = \varphi k_a \left|\boldsymbol{u}^*_{ai}\right| \boldsymbol{u}^*_{ai} - \varphi k_o \left|\boldsymbol{u}^*_{io}\right| \boldsymbol{u}^*_{io}, \tag{A1a}$$

$$|\boldsymbol{u}^*_{o}| \boldsymbol{u}^*_{o} = (1-\varphi)\beta \left|\boldsymbol{u}^*_{ai}\right| \boldsymbol{u}^*_{ai} + \varphi \left|\boldsymbol{u}^*_{io}\right| \boldsymbol{u}^*_{io}. \tag{A1b}$$

Here we have combined Eqs. (6a) and (6b) to relate the atmosphere–ice and atmosphere–ocean stress velocities via $\boldsymbol{u}^*_{ai}/\sqrt{C_{ai}} = \boldsymbol{u}^*_{ao}/\sqrt{C_{ao}}$. Equations (A1a–b) may in principle be solved analytically following a procedure similar to that described in Sect. 2.2: by defining stress velocity components parallel and perpendicular to the atmospheric velocity, $u^{*\parallel}_{io}$, $u^{*\perp}_{io}$, $u^{*\parallel}_{o}$, and $u^{*\perp}_{o}$, analogously to definitions Eqs. (13a) and (13b). Then taking the dot product of $\boldsymbol{u}^*_{ai}$ and $\hat{Z} \times \boldsymbol{u}^*_{ai}$ with each of Eqs. (A1a) and

TCD
9, 2101–2133, 2015

(A1b) yields four scalar equations that can be solved simultaneously for the components of $\boldsymbol{u}_{io}^{*}$ and $\boldsymbol{u}_{o}^{*}$. Finally, using the definitions $\left|\boldsymbol{u}_{io}^{*}\right|^2 = \left(u_{io}^{*\parallel}\right)^2 + \left(u_{io}^{*\perp}\right)^2$ and $|\boldsymbol{u}_{o}^{*}|^2 = \left(u_{o}^{*\parallel}\right)^2 + \left(u_{o}^{*\perp}\right)^2$ yields a pair of equations that must be solved simultaneously for $\left|\boldsymbol{u}_{io}^{*}\right|$ and $|\boldsymbol{u}_{o}^{*}|$. In practice we simply solve Eqs. (A1a–b) numerically using least-squares optimization.

Acknowledgements. H.-S. Park would like to thank S. Lee, S.-W. Son, Y. Kosaka and S. Feldstein for helpful comments and discussions. H.-S. Park was supported by the Basic Research Project of the Korea Institute of Geoscience and Mineral Resources (KIGAM) funded by the Ministry of Knowledge Economy of Korea. A. L. Stewart was supported by the University of California, Los Angeles, USA. The authors thank John Toole and Sylvia Cole for assistance with the ITP-V 35 observational dataset.

References

Bitz, C. M. and Polvani, L. M.: Antarctic climate response to stratospheric ozone depletion in a fine resolution ocean climate model, Geophys. Res. Lett., 39, L20705, doi:10.1029/2012GL053393, 2012.

Bitz, C. M., Fyfe, J., and Flato, G.: Sea ice response to wind forcing from AMIP models, J. Climate, 15, 522–536, 2002.

Cole, S. T., Timmermans, M.-L., Toole, J. M., Krishfield, R. A., and Thwaites, F. T.: Ekman veering, internal waves, and turbulence observed under Arctic Sea Ice, J. Phys. Oceanogr., 44, 1306–1328, 2014.

Dee, D. P., Uppala, S. M., Simmons, A. J., Berrisford, P., Poli, P., Kobayashi, S., Andrae, U., Balmaseda, M. A., Balsamo, G., Bauer, P., Bechtold, P., Beljaars, A. C. M., van de Berg, L., Bidlot, J., Bormann, N., Delsol, C., Dragani, R., Fuentes, M., Geer, A. J., Haimberger, L., Healy, S. B., Hersbach, H., Hólm, E. V., Isaksen, L., Kållberg, P., Köhler, M., Matricardi, M., McNally, A. P., Monge-Sanz, B. M., Morcrette, J.-J., Park, B.-K., Peubey, C., de Rosnay, P., Tavolato, C., Thépaut, J.-N., and Vitart, F.: The ERA-Interim reanalysis: configuration and performance of the data assimilation system, Q. J. Roy. Meteorol. Soc., 137, 553–597, 2011.

TCD
9, 2101–2133, 2015

Gray, J. M. N. T. and Morland, L. W.: A two-dimensional model for the dynamics of sea ice, Philos. T. Roy. Soc. A, 347, 219–290, 1994.
Heorton, D. B. S., Feltham, D. L., and Hunt, J. C. R.: The response of the sea ice edge to atmospheric and oceanic jet formation, J. Phys. Oceanogr., 44, 2292–2316, 2014.
Hibler III, W. D.: A dynamic thermodynamic sea ice model, J. Phys. Oceanogr., 9, 815–846, 1979.
Holland, P. R. and Kwok, R.: Wind-driven trends in Antarctic sea-ice drift, Nat. Geosci., 5, 872–875, 2012.
Kawakuchi, Y. and Mitsudera, H.: A numerical study of ice-drift divergence by cyclonic wind with a Lagrangian ice model, Tellus A, 60, 789–802, 2008.
Lee, S., Gong, T. T., Johnson, N. C., Feldstein, S. B., and Pollard, D.: On the possible link between tropical convection and the Northern Hemisphere Arctic surface air temperature change between 1958–2001, J. Climate, 24, 4350–4367, 2011.
Leppäranta, M.: The Drift of Sea Ice, Springer-Verlag, Berlin, 2005.
Li, X., Holland, D. M., Gerber, E. P., and Yoo, C.: Impacts of the north and tropical Atlantic Ocean on the Antarctic Peninsula and sea ice, Nature, 505, 538–542, 2014.
Liptak, J. and Strong, C.: The winter atmospheric response to sea ice anomalies in the Barents Sea, J. Climate, 27, 914–924, 2013.
Lüpkes, C. and Birnbaum, G.: Surface drag in the Arctic marginal sea-ice zone: a comparison of different parameterisation concepts, Bound.-Lay. Meteorol., 117, 179–211, 2005.
Lüpkes, C., Gryanik, V. M., Hartmann, J., and Andreas, E. L.: A parametrization, based on sea ice morphology, of the neutral atmospheric drag coefficients for weather prediction and climate models, J. Geophys. Res., 117, D13112, doi:10.1029/2012JD017630, 2012.
McPhee, M. G.: The effect of the oceanic boundary layer on the mean drift of pack ice: application of a simple model, J. Phys. Oceanogr., 9, 388–400, 1979.
McPhee, M. G.: An analytic similarity theory for the planetary boundary layer stabilized by surface buoyancy, Bound.-Lay. Meteorol., 21, 325–339, 1981.
McPhee, M. G.: On the turbulent mixing length in the oceanic boundary layer, J. Phys. Oceanogr., 24, 2014–2031, 1994.
McPhee, M. G. and Morison, J. H.: Under-ice Boundary Layer. Encyclopedia of Ocean Sciences, Academic Press, London, 3069–3076, 2001.
McPhee, M. G.: Air-Ice–Ocean Interaction: Turbulent Ocean Boundary Layer Exchange Processes, Chapt. 4 and 9, Springer, Berlin, 2008.

TCD
9, 2101–2133, 2015

McPhee, M. G.: Advances in understanding ice–ocean stress during and since AIDJEX, Cold Reg. Sci. Technol., 76, 24–36, 2012.
Ogi, M. and Wallace, J. M.: The role of summer surface wind anomalies in the summer Arctic sea ice extent in 2010 and 2011, Geophys. Res. Lett., 39, L09704, doi:10.1029/2012GL051330, 2012.
Pedlosky, J.: Geophysical Fluid Dynamics, 2nd Edn., Springer-Verlag, New York, Berlin, 227–232, 1987.
Plueddemann, A. J., Krishfield, R., Takizawa, T., Hatakeyama, K., and Honjo, S.: Upper ocean velocities in the Beaufort Gyre, Geophys. Res. Lett., 25, 183–186, 1998.
Raphael, M. N. and Hobbs, W.: The influence of the large-scale atmospheric circulation on Antarctic sea ice during ice advance and retreat seasons, Geophys. Res. Lett., 41, 5037–5045, doi:10.1002/2014GL060365, 2014.
Serreze, M. C., Maslanik, J. A., Scambos, T. A., Fetterer, F., Stroeve, J., Knowles, K., Fowler, C., Drobot, S., Barry, R. G., and Haran, T. M.: A record minimum arctic sea ice extent and area in 2002, Geophys. Res. Lett., 30, 1110, doi:10.1029/2002GL016406, 2003.
Smith, R. D., Dukowicz, J. K., and Malone, R. C.: Parallel ocean general circulation modeling, Physica D, 60, 38–61, 1992.
Sorteberg, A. and Kvingedal, B.: Atmospheric forcing on the Barents Sea winter ice extent, J. Climate, 19, 4772–4784, 2006.
Swift, C. T. and Cavalieri, D. J.: Passive microwave remote sensing for sea ice research, Eos Trans. AGU, 66, 1210–1212, 1985.
Thorndike, A. S. and Colony, R.: Sea ice motion in response to geostrophic winds, J. Geophys. Res., 87, 5845–5852, 1982.
Toole, J. M., Timmermans, M.-L., Perovich, D. K., Krishfield, R. A., Proshutinsky, A., and Richter-Menge, J. A.: Influences of the ocean surface mixed layer and thermohaline stratification on Arctic sea ice in the central Canada Basin, J. Geophys. Res., 115, C10018, doi:10.1029/2009JC005660, 2010.
Uotila, P., O'Farrell, S., Marsland, S. J., and Bi, D.: A sea-ice sensitivity study with a global ocean-ice model, Ocean Model., 51, 1–18, 2012.
Wettstein, J. J. and Deser, C.: Internal variability in projections of twenty-first-century arctic sea ice loss: role of the large-scale atmospheric circulation, J. Climate, 27, 527–550, 2014.

TCD
9, 2101–2133, 2015

Williams, A. J., Thwaites, F. T., Morrison, A. T., Toole, J. M., and Krishfield, R.: Motion tracking in an acoustic point-measurement current meter, Proc. OCEANS 2010 IEEE, Sydney, Australia, IEEE, 1–8, doi:10.1109/OCEANSSYD.2010.5603862, 2010.

Wu, B., Wang, J., and Walsh, J. E.: Dipole anomaly in the winter Arctic atmosphere and its association with sea ice motion, J. Climate, 19, 210–225, 2006.

Zhang, J. and Rothrock, D. A.: Modeling global sea ice with a thickness and enthalpy distribution model in generalized curvilinear coordinates, Mon. Weather Rev., 131, 681–697, 2003.

TCD
9, 2101–2133, 2015

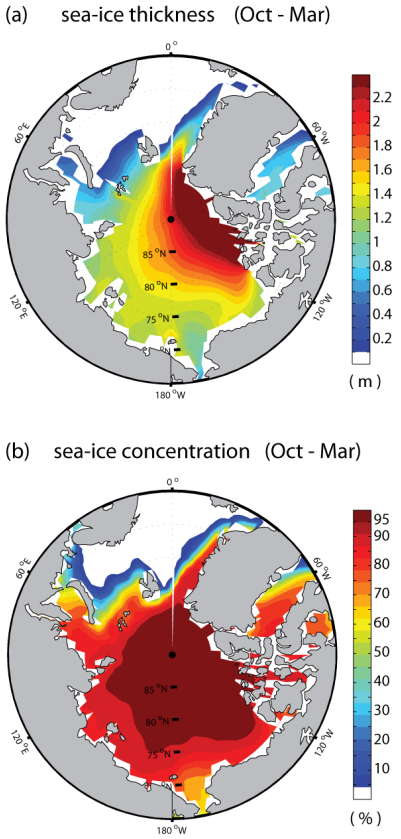

Figure 1. (a) Sea-ice thickness (m) and **(b)** sea-ice concentration (%), averaged from October 2009 to March 2010. Sea-ice thickness is from PIOMAS and sea-ice concentration data is from NSDIC.

TCD
9, 2101–2133, 2015

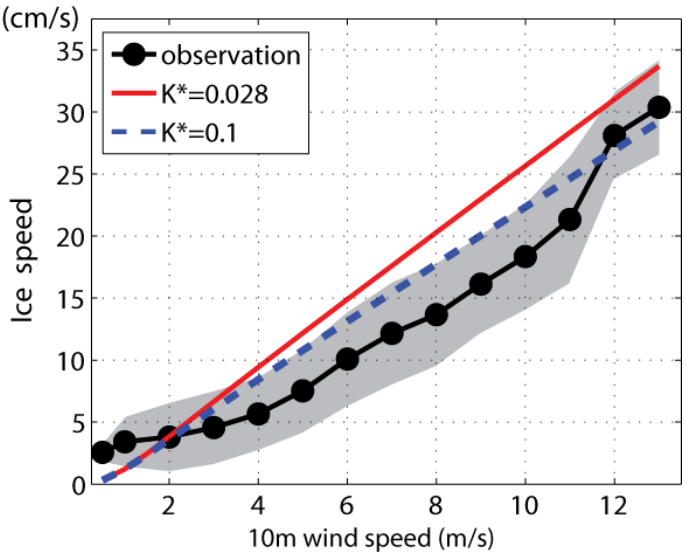

Figure 2. Sensitivity of ice speed ($m\,s^{-1}$) to 10 m wind speed ($m\,s^{-1}$). The black line shows the mean value calculated from ITP-V 35 observations binned by 10 m wind speed, and the gray shadings indicate the range of one standard deviation from the mean. The red and blue lines correspond to our analytical model, described in Sect. 2, with vertical diffusivities $K_o^* = 0.028$ and 0.1 respectively. The bulk sea-ice thickness is taken to be 1.5 m.

TCD
9, 2101–2133, 2015

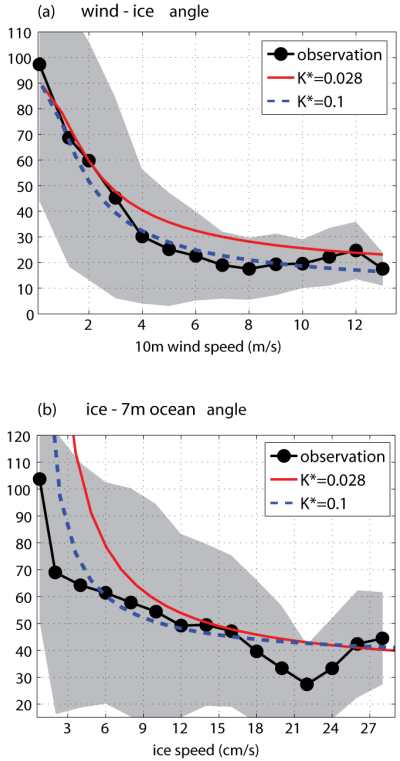

Figure 3. The velocity angle (clock-wise rotation angle) **(a)** between the 10 m winds and the ITPV-35 ice floe, and **(b)** between the ice floe and the ocean velocity at 7 m depth, as functions of the 10 m wind speed ($m\,s^{-1}$) and ice speed ($cm\,s^{-1}$) respectively. Note that typically the ice velocity lies to the right of the wind velocity, and the ocean velocity again lies to the right of the ice velocity. In each plot the black line is mean observed value from the ITP-V 35 dataset, binned by wind speed and ice speed respectively, and the gray shadings indicate the range of one SD from the mean. The red and blue lines correspond to our analytical model, described in Sect. 2, with vertical diffusivities $K_o^* = 0.028$ and 0.1 respectively.

TCD
9, 2101–2133, 2015

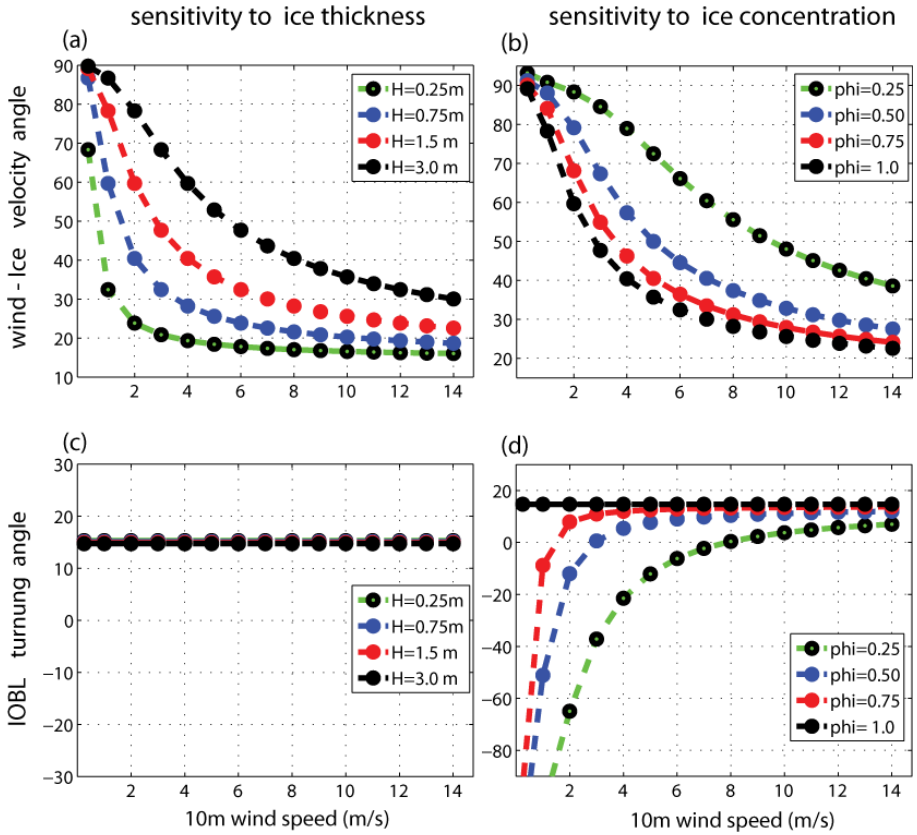

Figure 4. Analytical model sensitivity to various parameters: sensitivity of **(a, b)** wind–ice velocity angle and **(c, d)** IOBL turning angle to various values of **(a, c)** sea-ice thickness h_i (m) and **(b, d)** sea-ice concentration (φ) as a function of 10 m wind speed (abscissa; m s^{-1}). In all panels the dimensionless vertical diffusivity is fixed at $K_o^* = 0.028$. In **(a, c)** we use 100 % sea ice concentration ($\varphi = 1$), and in **(b, d)** we use a sea ice thickness of $h_i = 1.5$ m.

TCD
9, 2101–2133, 2015

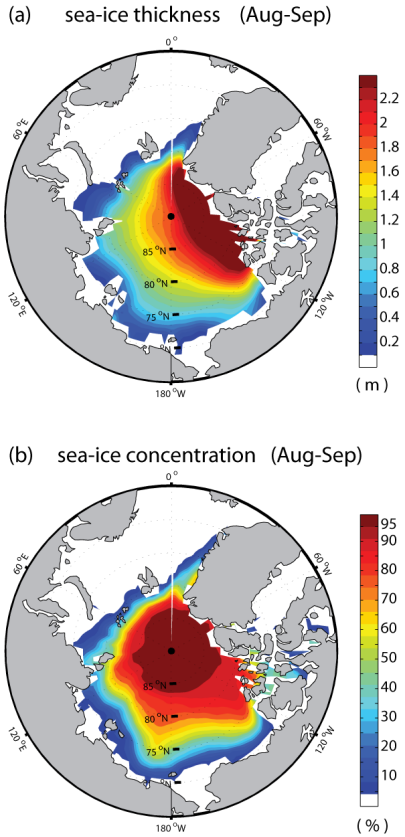

Figure 5. August-September climatological mean **(a)** sea-ice thickness (m) and **(b)** sea-ice concentration (%) during the years of 1990–2012. Sea-ice thickness is from PIOMAS and sea-ice concentration data is from NSDIC.

TCD
9, 2101–2133, 2015

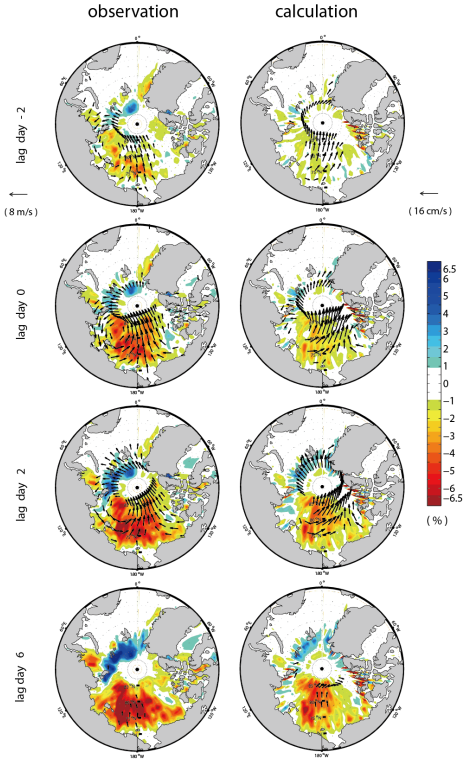

Figure 6. Composites of the anomalous sea-ice concentration (%) calculated from NSIDC satellite observations (left column) and from our analytical model using ERA-Interim 10 m wind velocity data (right column) for lag −2 days (first row), 0 days (second row), 2 day (third row), and lag +6 days (fourth row). See Sect. 5 for a full description of this calculation. Vectors indicate the anomalous 10 m winds from reanalysis ($m\,s^{-1}$; left column) and calculated sea-ice velocity ($cm\,s^{-1}$; right column). For surface winds (left column) and sea ice velocity (right column), only vectors stronger than $1.5\,m\,s^{-1}$ and $3.0\,cm\,s^{-1}$ are plotted respectively.

TCD
9, 2101–2133, 2015

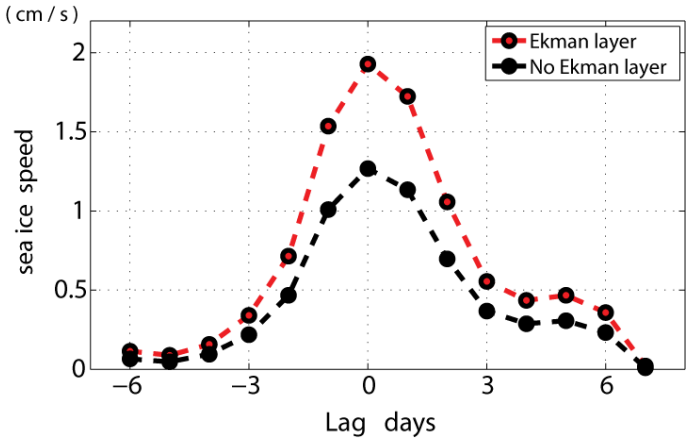

Figure 7. Lagged composite of the calculated sea-ice speed ($cm\,s^{-1}$) associated with the strong southerly events in the presence (red line) and in the absence (black line) of a surface Ekman layer in our analytical model (in the absence of an Ekman layer the ocean surface velocity is simply set to zero). The sea-ice speed is area-averaged over the Pacific sector of the Arctic (from 150 to 230° E and from 70 to 90° N). The sea ice speeds that include the surface Ekman layer (red line) identical to those used to construct Fig. 6. The dimensionless vertical diffusivity is $K_o^* = 0.028$ for the IOBL (red line).

TCD
9, 2101–2133, 2015